Comparison of the Luminous Efficiencies of Ga- and N-Polar $In_xGa_{1-x}N/In_yGa_{1-y}N$ Quantum Wells Grown by Plasma-Assisted Molecular Beam Epitaxy

Sergio Fernández-Garrido,[1,*] Jonas Lähnemann,[1,†] Christian Hauswald,[1,‡] Maxim Korytov,[2,§] Martin Albrecht,[2] Caroline Chèze,[3,‖] Czesław Skierbiszewski,[3,4] and Oliver Brandt[1]

[1]*Paul-Drude-Institut für Festkörperelektronik, Hausvogteiplatz 5–7, 10117 Berlin, Germany*
[2]*Leibniz-Institut für Kristallzüchtung, Max-Born-Strasse 2, 12489 Berlin, Germany*
[3]*TopGaN sp. z.o.o., al. Prymasa Tysiąclecia 98, 01-424 Warszawa, Poland*
[4]*Institute of High Pressure Physics, Polish Academy of Sciences, ul. Sokolowska 29/37, 01-142 Warszawa, Poland*

(Received 10 February 2016; revised manuscript received 15 June 2016; published 27 September 2016)

We investigate the luminescence of Ga- and N-polar $In_xGa_{1-x}N/In_yGa_{1-y}N$ quantum wells grown by plasma-assisted molecular beam epitaxy on freestanding GaN as well as 6*H*-SiC substrates. In striking contrast to their Ga-polar counterparts, the N-polar quantum wells prepared on freestanding GaN do not exhibit any detectable photoluminescence even at 10 K. Theoretical simulations of the band profiles combined with resonant excitation of the quantum wells allow us to rule out carrier escape and subsequent surface recombination as the reason for this absence of luminescence. To explore the hypothesis of a high concentration of nonradiative defects at the interfaces between wells and barriers, we analyze the photoluminescence of Ga- and N-polar quantum wells prepared on 6*H*-SiC as a function of the well width. Intense luminescence is observed for both Ga- and N-polar samples. As expected, the luminescence of the Ga-polar quantum wells quenches and redshifts with increasing well width due to the quantum confined Stark effect. In contrast, both the intensity and the energy of the luminescence from the N-polar samples are essentially independent of the well width. Transmission electron microscopy reveals that the N-polar quantum wells exhibit abrupt interfaces and homogeneous composition, excluding emission from In-rich clusters as the reason for this anomalous behavior. The microscopic origin of the luminescence in the N-polar samples is elucidated using spatially resolved cathodoluminescence spectroscopy. Regardless of well width, the luminescence is found to not originate from the N-polar quantum wells but from the semipolar facets of ∨-pit defects. These results cast serious doubts on the potential of N-polar $In_xGa_{1-x}N/In_yGa_{1-y}N$ quantum wells grown by plasma-assisted molecular beam epitaxy for the development of long-wavelength light-emitting diodes.

DOI: 10.1103/PhysRevApplied.6.034017

I. INTRODUCTION

The growth of $In_xGa_{1-x}N$ alloys along the $[000\bar{1}]$ direction (known as N-polar orientation) with high In content has regained interest because it offers potential advantages for the fabrication of green light-emitting diodes (LEDs). Despite the rougher surfaces and higher concentrations of impurities in N-polar group-III nitride films as compared to their Ga-polar (i.e., [0001]-oriented) counterparts grown under identical conditions [1–5], the $[000\bar{1}]$ orientation offers two interesting advantages. The first of these advantages is an enhanced In-incorporation efficiency [5,6]. This phenomenon is the result of the higher thermal stability of N-polar InN and paves the way for the use of significantly higher substrate temperatures [7] that may help improve the crystal quality as well as minimize the incorporation of impurities. The second advantage is related to the expected improvement in device performance caused by the reversed direction of the polarization fields in the quantum wells (QWs) that constitute the active region of LEDs. As discussed in Ref. [8], this fact should result in lower turn-on voltages and higher internal quantum efficiencies. Unlike other epitaxial growth techniques, where the incorporation of high In content is challenging due to the low decomposition efficiency of NH_3 at reduced substrate temperatures [9], plasma-assisted molecular beam epitaxy (PAMBE) facilitates the synthesis of $In_xGa_{1-x}N$ alloys across the entire compositional range [10–12].

Inspired by the potential advantages of N-polar $In_xGa_{1-x}N$ alloys, Akyol *et al.* [13] demonstrated the PAMBE growth of N-polar $In_xGa_{1-x}N$ LEDs emitting at 540 nm in 2011. However, in contrast to this encouraging

*garrido@pdi-berlin.de
†Present address: Equipe mixte CEA-CNRS-UJF Nanophysique et Semiconducteurs, INAC/SP2M, CEA-Grenoble, 17 rue des Martyrs, 38054 Grenoble, France.
‡Present address: DILAX Intelcom GmbH, Alt-Moabit 96b, 10559 Berlin, Germany.
§Present address: CEMES-CNRS and Université de Toulouse, 29 rue Jeanne Marvig, F-31055 Toulouse, France.
‖Present address: Paul-Drude-Institut für Festkörperelektronik, Hausvogteiplatz 5–7, 10117 Berlin, Germany.

work, some disconcerting results have been recently reported by Chèze *et al.* [4] who analyzed the optical properties of $In_xGa_{1-x}N/In_yGa_{1-y}N$ QWs grown by PAMBE along the [0001] and $[000\bar{1}]$ directions. Despite a comparable structural and morphological quality of their Ga- and N-polar QWs, the latter did not exhibit any detectable photoluminescence (PL) associated with the $In_xGa_{1-x}N/In_yGa_{1-y}N$ QWs. In contrast, an unclad *thick* (150-nm) N-polar $In_xGa_{1-x}N$ layer grown under identical conditions did show intense emission in the red spectral range. Therefore, Chèze *et al.* [4] attributed the lack of luminescence in the N-polar QWs to either surface-induced electric fields causing carriers to escape from the QWs and to subsequently recombine at the surface nonradiatively or to a high concentration of nonradiative defects located at the interfaces between wells and barriers. The poor luminous efficiency of N-polar $In_xGa_{1-x}N$ QWs does not seem to be a specific problem of PAMBE but has also been reported for N-polar $In_xGa_{1-x}N/In_yGa_{1-y}N$ QWs grown by metal organic chemical vapor deposition (MOCVD) [3,14,15]. Also, for the case of MOCVD, this phenomenon is not understood yet but has been tentatively attributed to higher dislocation densities [14] as well as elevated residual impurity concentrations [3,14].

In this work, we investigate the luminescence of Ga- and N-polar $In_xGa_{1-x}N/In_yGa_{1-y}N$ QWs to find a consistent explanation for the differences in their efficiencies. Carrier escape and surface recombination are ruled out by combining simulations of the band profiles with PL measurements carried out with resonant excitation. To explore the remaining possibility, namely, the presence of a high concentration of nonradiative defects at the interfaces between wells and barriers, we analyze Ga- and N-polar QWs with different widths. The PL spectra of Ga-polar QWs exhibit the expected behavior, i.e., they quench and redshift with increasing QW width. For the N-polar samples, we observe an intense emission whose intensity and energy do not depend on the QW width. The analysis of the N-polar QWs by transmission electron microscopy (TEM) reveal a random alloy composition and the absence of clustering. The anomalous behavior of the PL is, thus, not caused by the localization of excitons at alloy inhomogeneities. The actual origin of the luminescence is clarified using spatially resolved cathodoluminescence (CL) spectroscopy. These measurements show that regardless of the QW width, the luminescence does not arise from the N-polar QWs themselves but from semipolar ones formed in ∨-pit defects.

II. EXPERIMENTS AND METHODS

The samples used in this study are independently prepared by two groups (TopGaN and PDI) using different PAMBE systems and substrates. Samples *A* and *B* are prepared at TopGaN. They are grown in a V90 VG Semicon MBE system equipped with two Veeco UNI-Bulb radio-frequency N_2 plasma sources for active N and solid-source effusion cells for Ga and In. The two samples contain three $In_xGa_{1-x}N/In_yGa_{1-y}N$ QWs grown side by side on GaN substrates of different polarity. Sample *A* is grown on a bulk GaN(0001) crystal produced by high nitrogen pressure solution synthesis and sample *B* on a freestanding $GaN(000\bar{1})$ layer prepared by hydride vapor phase epitaxy. The threading dislocation (TD) densities of the substrates used for the growth of samples *A* and *B* are on the order of 10^3 and 10^7 cm^{-2}, respectively. Note that even the latter TD density is significantly smaller than the one tolerated in commercial LEDs [16–18]. Prior to the growth, the substrates are outgassed at 650 °C for 60 min in the preparation chamber of the MBE system. After transferring the substrates into the growth chamber, a 100-nm-thick GaN layer is grown under intermediate metal-stable growth conditions [19] to ensure a smooth growth front as well as to bury residual surface contaminations. This GaN layer is grown at 730 °C, and the Ga and N fluxes are 6.7×10^{14} and 4×10^{14} atoms $cm^{-2}\,s^{-1}$, respectively. Afterwards, the substrate temperature is decreased to 660 °C for the growth of the QW region. Just before growing the QWs, we insert a 33-nm-thick $In_yGa_{1-y}N$ layer grown using the same conditions as for the $In_yGa_{1-y}N$ quantum barriers (QBs) (see below) to keep away the quantum-well region from the interface formed after interrupting the growth to lower the substrate temperature. Furthermore, this layer also guarantees stable growth conditions before initiating the growth of the $In_xGa_{1-x}N/In_yGa_{1-y}N$ QWs. Both the nominally 3-nm-thick $In_xGa_{1-x}N$ QWs and 7-nm-thick $In_yGa_{1-y}N$ QBs are grown within the metal-rich growth regime in which droplet formation occurs [20]. The Ga and N fluxes for the growth of the QWs (QBs) are 7.4×10^{14} (4×10^{14}) and 1×10^{15} (4.2×10^{14}) atoms $cm^{-2}\,s^{-1}$, respectively. The fluxes are varied between the QWs and the QBs by opening and closing the shutters of two different N_2 plasma sources and Ga effusion cells. The In flux adjusted to ensure a slight accumulation of metal in the form of In droplets is kept constant during the growth of the QWs and QBs. The nominal In content in the $In_yGa_{1-y}N$ layer as well as in the QBs is kept below 3%. As explained in detail in Ref. [21], the incorporation of In into the barriers facilitates the uninterrupted two-dimensional growth of QWs and QBs under metal-stable growth conditions. The In content in the barriers is, nevertheless, sufficiently low to guarantee a suitable degree of confinement of electrons and holes inside the $In_xGa_{1-x}N$ QWs. Finally, the QWs are capped with a 17-nm-thick $In_yGa_{1-y}N$ layer grown under the same conditions as the QBs. After the growth, the excess In on the surface is removed by HCl etching. The structural parameters of the QWs and QBs, as determined by high-resolution x-ray diffraction [4] (HRXRD), are summarized in Table I. The higher In content in the QWs of sample *B* is the result of the

TABLE I. Substrates as well as widths d and In contents x determined by HRXRD and TEM of the QWs and QBs for all the samples presented in this work. The errors in the values of x for samples A–F and G–J are 0.005 and 0.015, respectively.

Sample	Substrate	d_{QW} (nm)	x_{QW}	d_{QB} (nm)	x_{QB}
A	Bulk GaN(0001)	2.5	0.13	6.3	0.01
B	FS − GaN(000$\bar{1}$)	3.1	0.23	6.3	0.01
C	6H − SiC(0001)	2.9	0.14	9.5	0.02
D	6H − SiC(0001)	5.6	0.14	9.1	0.02
E	6H − SiC(0001)	8	0.13	9	0.03
F	6H − SiC(0001)	10.6	0.13	8.9	0.02
G	6H − SiC(000$\bar{1}$)	3	0.19	9.5	0.02
H	6H − SiC(000$\bar{1}$)	5.8	0.24	9.5	0.01
I	6H − SiC(000$\bar{1}$)	8.4	0.22	9.5	0.02
J	6H − SiC(000$\bar{1}$)	11.2	0.20	9.5	0.01

enhanced In incorporation observed for [000$\bar{1}$]-oriented films [4,6,7]. As shown in Ref. [4], the two samples have atomically smooth surfaces characterized by single atomic steps and root-mean-square (rms) roughness values well below 1 nm. The combined analysis of the samples by TEM and HRXRD reveal that the QWs exhibit sharp interfaces and are free of misfit dislocations. More details about the growth conditions and properties of these samples can be found elsewhere [4].

Two additional series of samples (C–F and G–J) are grown at PDI in a custom-designed CREATEC PAMBE system equipped with a Vecco UNI-Bulb radio-frequency plasma source for the generation of active N and solid-source effusion cells for Ga and In. Samples C–F contain five Ga-polar $In_xGa_{1-x}N/In_yGa_{1-y}N$ QWs prepared on 6H-SiC(0001) substrates. The other samples (G–J) contain nominally identical structures on 6H − SiC(000$\bar{1}$); i.e., they are of opposite polarity [5,22]. The typical TD density of GaN layers grown by PAMBE on 6H-SiC is on the order of 10^{10} cm^{-2} [5,23]. The backside of the substrates is coated with Ti for efficient heat absorption during growth. The as-received SiC substrates are prepared following the procedure described in Ref. [24]. Prior to the growth of the $In_xGa_{1-x}N/In_yGa_{1-y}N$ QWs, a 1-μm-thick GaN layer is grown under intermediate metal-stable growth conditions at 690 °C [19]. The Ga and N fluxes used for the growth of this layer are 7.2×10^{14} and 5×10^{14} atoms cm^{-2} s^{-1}, respectively. Afterwards, the substrate temperature is decreased to 625 °C to grow the QW region. Similar to the case of samples A and B, we prepare a 100-nm-thick $In_yGa_{1-y}N$ ($y < 0.03$) layer before growing the $In_xGa_{1-x}N/In_yGa_{1-y}N$ QWs. For the subsequent uninterrupted growth of QWs and QBs, the N and In fluxes are kept constant. Their values are 5×10^{14} and 4.3×10^{14} atoms cm^{-2} s^{-1}, respectively. The Ga flux is reduced to grow the $In_xGa_{1-x}N$ QWs by closing the shutter of one of the two Ga cells used in these experiments, from 4.7×10^{14} to 3.5×10^{14} atoms cm^{-2} s^{-1}. In contrast to samples A and B, samples C–J are grown under intermediate metal-stable growth conditions, i.e., avoiding the formation of In droplets. For all of these samples, the nominal width of the QBs and the thickness of the final cap layer (grown under the same conditions as the QBs) are 10.1 and 30 nm, respectively. The nominal width of the QWs is varied for each type of substrate between 2.6 and 12 nm. Regardless of the QW width, we always observe a streaky reflection high-energy electron-diffraction pattern during the growth of the samples (not shown here).

The morphological and structural properties of samples C–J are also analyzed by atomic force microscopy (AFM) and HRXRD, respectively. HRXRD experiments are performed with $CuK_{\alpha 1}$ radiation (wavelength $\lambda = 1.54056$ Å) using a PANalytical X'Pert Pro MRD system equipped with a Ge(220) hybrid monochromator. Symmetric ω-2θ scans across the GaN 0002 Bragg reflection are measured with a three-bounce Ge(220) analyzer crystal. The experimental results are simulated using the dynamical x-ray diffraction model reported in Ref. [25]. To gain further insight into the structural properties of the samples, we use TEM. The cross-sectional TEM specimens are prepared by mechanical tripod polishing followed by Ar^+ milling until reaching electron transparency. All measurements are performed using an aberration-corrected FEI Titan 80–300 electron microscope operated at 300 keV.

The optical properties of the samples are investigated by low-temperature (10 K) μ-PL and CL spectroscopy. Depending on the well width, PL is excited using either the 413-nm line of a Kr^+ laser or the 473-nm line of a diode-pumped solid-state laser. In both cases, the PL is dispersed by an 80-cm HORIBA Jobin Yvon monochromator and detected by a charge-coupled-device detector. All measurements are corrected for the spectral response of the PL setup. CL measurements are performed at acceleration voltages of 3–5 kV using a Gatan MonoCL3 CL system equipped with a parabolic mirror for light collection and with both a photomultiplier and a charge-coupled device for detection mounted to a Zeiss Ultra-55 field-emission scanning electron microscope (SEM). Monochromatic images are taken with a spectral resolution window of 1–2 nm.

The band profiles and wave functions are computed using a self-consistent Schrödinger-Poisson solver [26]. To account for the different residual doping of Ga- and N-polar samples [4], we set the donor densities in samples A and B to 5×10^{16} and 1×10^{18} cm^{-3}, respectively. Fermi-level pinning at the surface is taken into account. In accordance with the results reported in Ref. [27], for our samples exposed to air, we assume that the Fermi level is pinned 0.6 and 0.27 eV below the conduction-band minimum for the Ga- and N-polar samples, respectively. Nevertheless, our results do not qualitatively depend on the value at which the Femi level is actually pinned [27,28]. The InN and GaN band gaps, as well as the bowing parameter used to estimate

the corresponding values of the $In_xGa_{1-x}N$ and $In_yGa_{1-y}N$ layers, are extracted from Refs. [29] and [30], respectively. For the electron and hole effective masses, we use the values recommended by Vurgaftman and Meyer [31]. To calculate the polarization fields, we use the parameters reported in Ref. [32] by Bernardini and Fiorentini.

III. RESULTS

A. Carrier escape and surface recombination as possible origin of the lack of PL in N-polar $In_xGa_{1-x}N/In_yGa_{1-y}N$ QWs

To investigate whether the lack of PL for N-polar $In_xGa_{1-x}N/In_yGa_{1-y}N$ QWs reported by Chèze *et al.* [4] may be caused by carrier escape from the QWs, we calculate the band profiles of Ga- and N-polar QWs and perform low-temperature (10 K) μ-PL experiments with resonant excitation.

1. Simulation of the band profiles

Figure 1 presents the simulated band profiles for the Ga- and N-polar QWs studied by Chèze *et al.* [4] (samples *A* and *B*). We also present the calculated ground-state electron and hole wave functions for the second QW. Similar results are obtained for the other two QWs (not shown here for clarity).

For the N-polar $In_xGa_{1-x}N/In_yGa_{1-y}N$ QWs (sample *B*), the electric field near the sample surface is stronger and of opposite direction compared to their Ga-polar counterparts. In the cap layer, electrons are, thus, pulled toward the surface, and the holes are dragged into the QW region. Because of the reverse direction of the piezoelectric fields, the direction of the electric field inside the QWs is also opposite for samples *A* and *B*. Because of this reason, electron and hole wave functions are localized in the QWs at opposite interfaces.

The simulations demonstrate that the electron and hole ground states are well confined into the QWs for both samples. To reach the surface, both electrons and holes have to overcome large barriers, particularly so for sample *B*. In fact, comparing the spatial extension of the wave functions, the confinement of both electrons and holes is seen to be significantly stronger in the QWs of sample *B* as a result of the reversed fields and the higher In content (see Table I). An escape of carriers from the QWs seems hardly possible for sample *A* but much less so for sample *B*.

Finally, we note that the overlap between the electron and hole wave functions is about a factor of 2 larger for sample *A* as compared to sample *B*. This reduction in overlap due to the slightly larger QW thickness as well as the stronger electric field caused by the higher In content could explain a corresponding quenching of the luminous efficiency (assuming an equally strong nonradiative participation in recombination) but certainly not the absolute lack of luminescence reported by Chèze *et al.* [4].

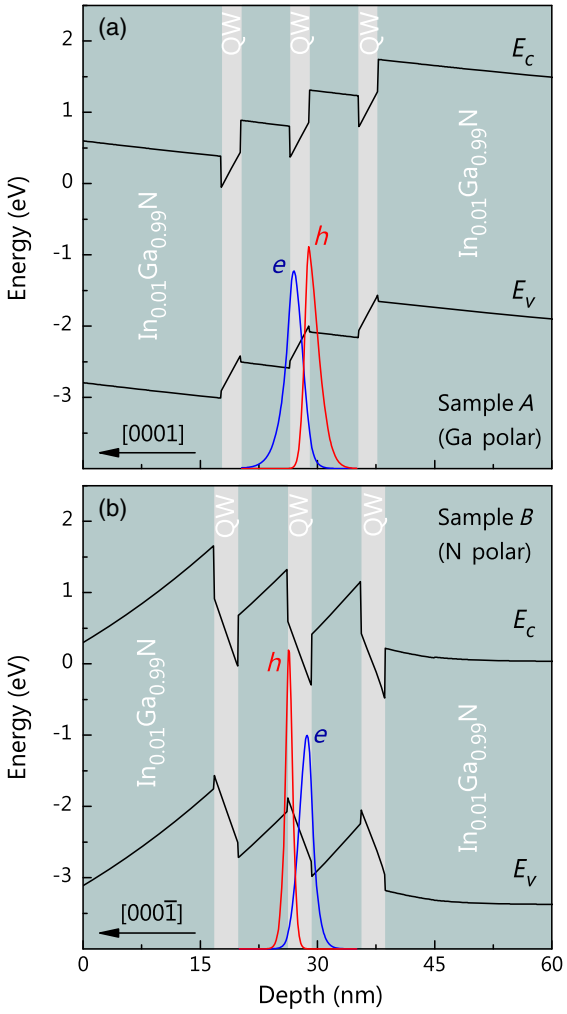

FIG. 1. Band profiles of the Ga-polar sample *A* (a) and the N-polar sample *B* (b). In both figures, we also show the calculated electron (solid blue line) and hole (solid red line) wave functions for the second QW.

2. Low-temperature photoluminescence with resonant excitation

The low-temperature (10 K) PL experiments reported by Chèze *et al.* [4] are performed using the 325-nm line of a He-Cd laser. For this wavelength, most carriers are not directly excited in the QWs but in the cap layer and the surrounding QBs. The QW emission may then be suppressed by nonradiative recombination in the QBs, competing with the capture of carriers by the QWs. To exclude this possibility, we here examine the PL spectra of samples *A* and *B* obtained by *direct* excitation at 413 nm.

Figure 2 shows the low-temperature PL spectra of samples *A* and *B* recorded with direct excitation. For sample *A*, we observe a strong emission at 2.75 eV as well as its longitudinal optical phonon replica from the Ga-polar $In_xGa_{1-x}N$ QWs. The yellow band centered at approximately 2.25 eV stems from the GaN substrate. For

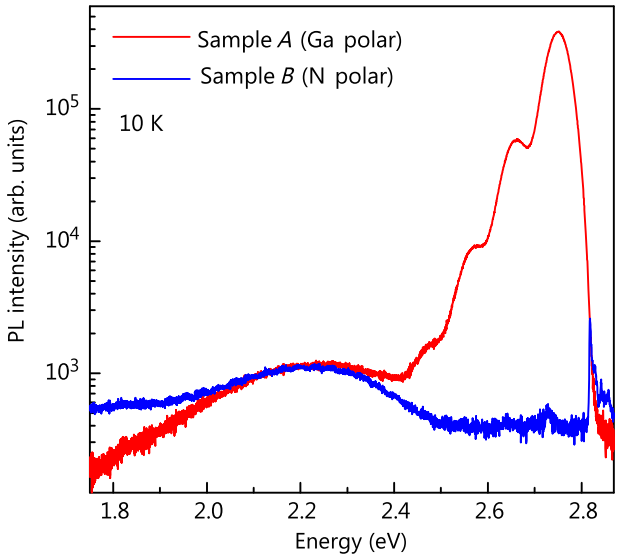

FIG. 2. Low-temperature (10 K) μ-PL spectra under resonant excitation (413 nm) of samples A and B. The samples are measured side by side with an excitation density of 200 and 2000 kW/cm^2 for samples A and B, respectively. The sharp feature at 2.82 eV for sample B originates from second-order optical phonon scattering in the GaN substrate. The spectra are vertically shifted to line up their background in order to account for the different integration times used during the measurements.

sample B, we observe only the yellow band at 2.25 eV and a sharp feature at 2.82 eV which originates from second-order optical phonon scattering but no emission line which could be associated to the N-polar $In_xGa_{1-x}N$ QWs.

B. Effect of quantum-well width on the properties of Ga- and N-polar $In_xGa_{1-x}N/In_yGa_{1-y}N$ QWs

The results presented in the previous section demonstrate the presence of an efficient nonradiative recombination channel within N-polar $In_xGa_{1-x}N/In_yGa_{1-y}N$ QWs. Because Chèze *et al.* [4] observed an intense luminescence from thick N-polar $In_xGa_{1-x}N$ layers grown under similar conditions (comparable to the intensity observed in Ga-polar $In_xGa_{1-x}N/In_yGa_{1-y}N$ QWs), the most plausible explanation for the lack of luminescence is a high concentration of nonradiative defects at the interfaces between QWs and QBs. Within the classical treatment of surface and interface recombination [33] and assuming a diffusion length much larger than the layer thickness, the nonradiative rate is expected to decrease linearly with the thickness of the layer. In the present case, the location of the charge carriers is determined not by diffusive transport but by drift in the strong internal electrostatic field within the $In_xGa_{1-x}N$ QWs, and it is, thus, doubtful whether this expectation still holds. To investigate this scenario, we analyze the luminescence of nominally identical Ga- and N-polar $In_xGa_{1-x}N/In_yGa_{1-y}N$ structures as a function of the width of the $In_xGa_{1-x}N$ QWs (samples C–J).

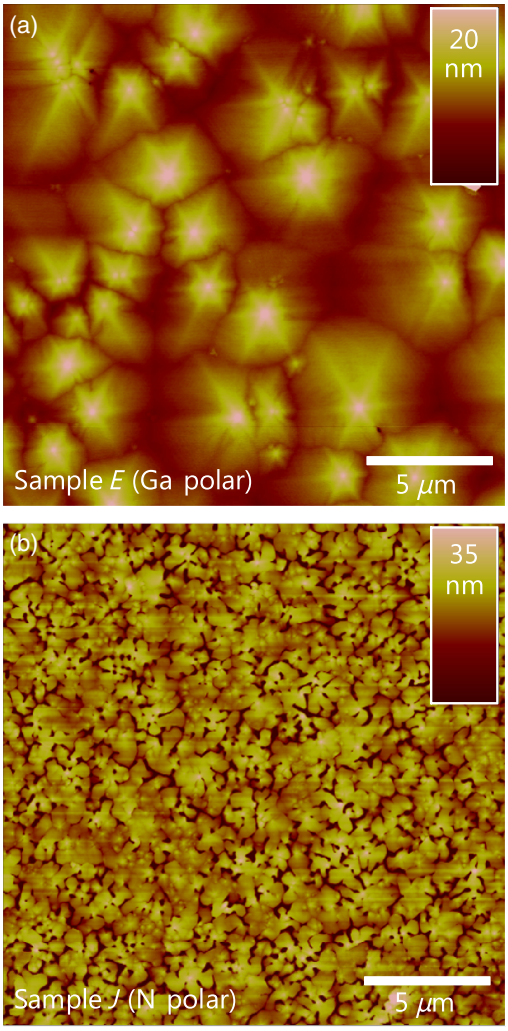

FIG. 3. Characteristic AFM images of Ga- (a) and N-polar (b) $In_xGa_{1-x}N/In_yGa_{1-y}N$ QWs on SiC{0001}. The images shown are taken from samples E (a) and J (b).

1. Morphological and structural characterization

The morphological and structural properties of the QW samples prepared on SiC are investigated by AFM and HRXRD. Figures 3(a) and 3(b) show characteristic 20×20 μm^2 AFM images of two QW samples grown along the [0001] and $[000\bar{1}]$ directions, respectively. For the Ga-polar QWs (samples C–F), the surfaces are characterized by atomic steps and hillocks. The latter originate from spiral step-flow growth around screw dislocations. The density of hillocks is on the order of approximately 1×10^7 cm^{-2} and the rms roughness is lower than 1 nm. The surfaces of the N-polar QWs (samples G–J) are much rougher with rms values as high as 8 nm. These larger values are primarily due to the presence of a high density of pits as shown in Fig. 3(b).

Figure 4 presents two exemplary ω-2θ scans performed to assess the In concentration as well as the widths of the QWs and QBs of the samples C–J. The figure also shows

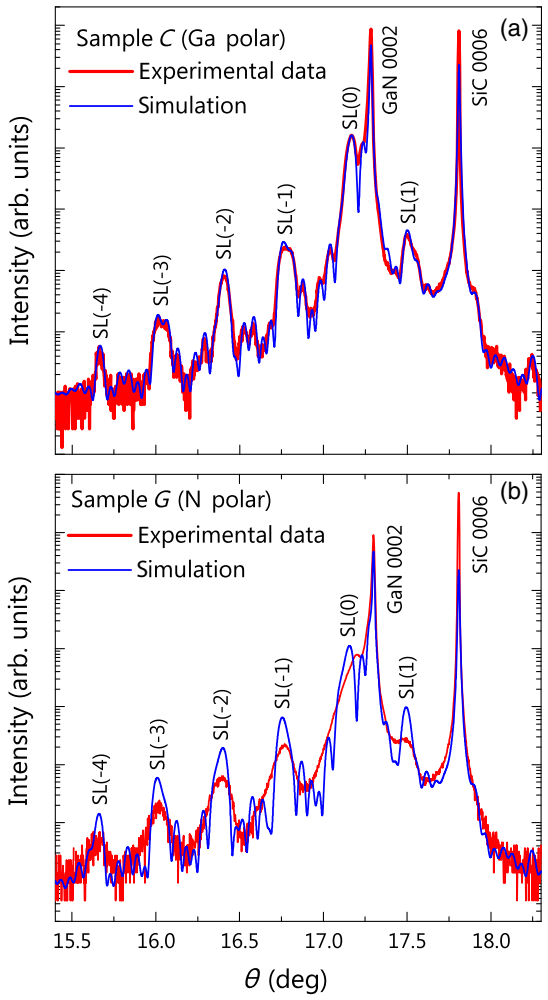

FIG. 4. Examples for experimental and simulated triple-crystal ω-2θ scans across the GaN 0002 reflection of Ga- (a) and N-polar (b) $In_xGa_{1-x}N/In_yGa_{1-y}N$ QWs on SiC{0001}. The scans are taken from samples *C* (a) and *G* (b).

the corresponding simulated HRXRD profiles. The parameters derived from the simulations, assuming that QWs and QBs have the same in-plane lattice constant as the GaN layer underneath, are summarized in Table I. For the Ga-polar $In_xGa_{1-x}N/In_yGa_{1-y}N$ QWs [Fig. 4(a)], we observe satellite peaks up to at least fourth order in addition to the dominant SiC 0006 and GaN 0002 reflections. The excellent agreement of experimental and simulated profiles including the complex interference fringes modulating the satellites reflects the high periodicity and the abrupt interfaces of the $In_xGa_{1-x}N/In_yGa_{1-y}N$ quintuple QW structure. The structural parameters for the Ga-polar samples *C*–*F* are, thus, obtained with high accuracy. For the N-polar $In_xGa_{1-x}N/In_yGa_{1-y}N$ QWs, we also observe satellite peaks up to fourth order [see Fig. 4(b)], but all satellites (including the zeroth-order one) are significantly broadened compared to the simulation. This broadening indicates a significant compositional variation within the structure. Because of this broadening, the error in the structural parameters obtained for the N-polar samples *G*–*J* is larger than for their Ga-polar counterparts. In order to minimize the error in the estimation of the In contents *x*, we simulate the HRXRD profiles of samples *G*–*J* using the QW and QB thicknesses derived from transmission electron micrographs (see Sec. III B 3). As shown in Table I, we consistently obtain higher values of *x* for samples *G*–*J* than for samples *C*–*F* [on average $(21.3 \pm 2.2)\%$ as compared to $(13.5 \pm 0.6)\%$]. This latter result reflects again the enhanced In incorporation efficiency along the $[000\bar{1}]$ direction [4,6,7].

2. *Low-temperature photoluminescence with resonant excitation*

Figure 5 presents the low-temperature (10 K) μ-PL spectra excited at 413 nm (473 nm for samples *E* and *F*) of the Ga- (a) and N-polar (b) $In_xGa_{1-x}N/In_yGa_{1-y}N$ QWs. For the Ga-polar samples [Fig. 5(a)], a strong

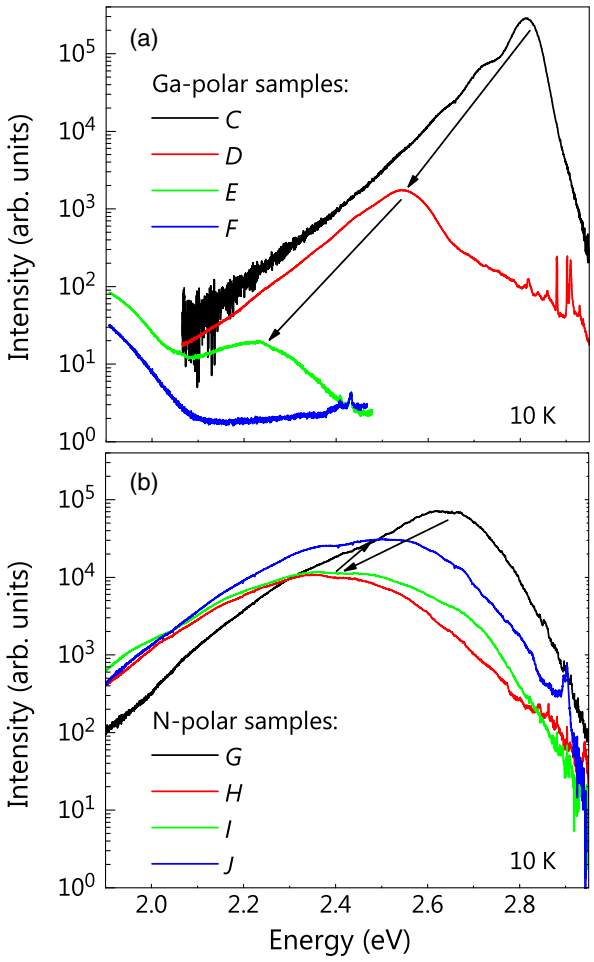

FIG. 5. Low-temperature (10 K) μ-PL spectra of Ga- (a) and N-polar (b) $In_xGa_{1-x}N/In_yGa_{1-y}N$ QWs with different widths. The arrows indicate the shift of the $In_xGa_{1-x}N$ peak with increasing QW width.

QW-related emission centered at 2.81 and 2.54 eV is observed for the two samples with the narrowest QWs, i.e., sample *C* and sample *D*, respectively. For sample *E*, the donor-acceptor-pair (N-Al) emission of SiC dominates the spectrum for excitation at 413 nm (not shown). When exciting with the 473-nm line, we detect a weak but clear emission from the $In_xGa_{1-x}N$ QWs centered at 2.23 eV. Finally, for sample *F*, we do not observe any emission that can be ascribed to the QWs. The luminescence band below 2 eV, which is also seen in the PL spectra of the other samples, is due to partial dislocations in faulted regions in the SiC substrate [34]. The N-polar samples, the spectra of which are shown in Fig. 5(b), behave completely different: for all samples, we detect a broad emission band much more intense than any emission from SiC. Neither the energy position nor the intensity of this band seem to depend systematically on QW width.

Figure 6 shows the energy *E* [Figs. 6(a) and 6(b)] and the integrated intensity *I* [Figs. 6(c) and 6(d)] of the $In_xGa_{1-x}N$ PL band as a function of the QW width *d* for the two series of samples. For comparison, we also display the transition energies between the single-particle electron and hole states as well as the absolute square of the electron-hole overlap integrals (assumed to be proportional to the integrated intensity) as determined by our Schrödinger-Poisson simulations using the structural parameters summarized in Table I. For the Ga-polar samples, both the transition energy and the intensity exhibits the expected and theoretically predicted trend, namely, the PL band redshifts linearly and quenches exponentially with increasing QW width due to the quantum-confined Stark effect (QCSE) [35]. For the N-polar samples, in contrast, the experimental and simulated results are in gross disagreement. Similar to the Ga-polar samples, the simulations predict a strong and monotonic redshift as well as an exponential quenching of the $In_xGa_{1-x}N$ emission with increasing QW width. Instead, both the transition energy and the intensity exhibit a weak nonmonotonic dependence on the QW width. Particularly remarkable is the fact that the N-polar samples are brighter than their Ga-polar counterparts with the sole exception of the sample with the thinnest QWs.

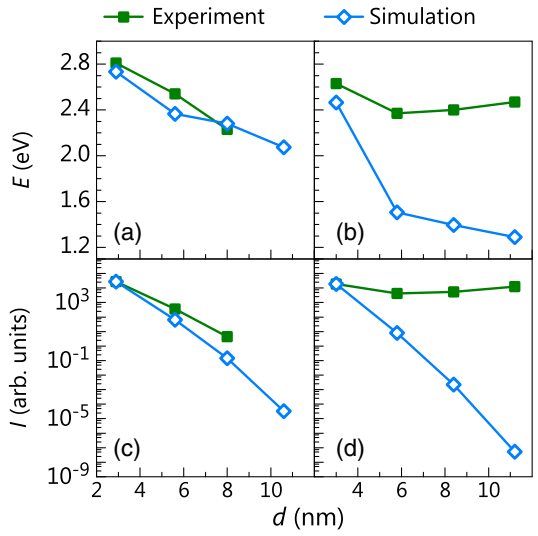

FIG. 6. (a),(b) Experimental (squares) and simulated (diamonds) transition energy *E* of the QW PL band as a function of the QW width *d* for the Ga- and N-polar samples, respectively. (c),(d) Experimental (squares) and simulated (diamonds) intensity *I* of the QW PL band for the Ga- and N-polar samples, respectively. The latter is obtained by scaling the calculated electron-hole overlap as described in the text.

These results are in striking contrast to those presented in Sec. III A 2 and those reported in Ref. [4]. The independence of PL energy and intensity on QW width observed for samples *G*-*J* can be understood if the emission is dominated by strongly localized states created by nonrandom alloy inhomogeneities [36–41]. Strong alloy fluctuations will also be consistent with the broadening of the satellite peaks observed in the triple-crystal ω-2θ scans discussed in Sec. III B 1. In the following, we, therefore, investigate the samples at a microscopic and nanometric scale by TEM. In addition, we attempt to unravel the microscopic origin of the emission observed by spatially resolved CL spectroscopy.

3. Transmission electron microscopy

To study the microscopic structure of the N-polar $In_xGa_{1-x}N/In_yGa_{1-y}N$ QWs, we analyze samples *G* and *I* by various TEM techniques. Weak-beam dark-field (WBDF) imaging is used to visualize the spatial distribution of different types of dislocations as well as to estimate TD densities. The atomic structure of the QWs is studied by high-angle annular dark-field scanning transmission electron microscopy (STEM HAADF). High-resolution TEM (HRTEM) is used for a structural analysis of the alloys on an atomic scale.

Figures 7(a)–7(c) show cross-sectional WBDF micrographs taken of sample *I* with different diffraction vectors. The micrographs show that some but not all of the TDs originating at the GaN/SiC interface affect the growth of the $In_xGa_{1-x}N/In_yGa_{1-y}N$ QWs and lead to the formation of $\vee$-pit defects also visible in the AFM images depicted in Fig. 3(b). The comparison of Figs. 7(a) and 7(b) reveals that the ratio between *c*- and *a*-type TDs is approximately 1:5, while their total areal density is in the range of $(1–4) \times 10^{10}$ cm^{-2}. This value is comparable to the typical TD densities reported in the literature for GaN layers grown on 6*H*-SiC [5,23]. Quite unexpectedly, Fig. 7(c) also reveals the presence of *a*-type misfit dislocations (MDs) in sample *I*, well below the onset of significant plastic relaxation of the entire film in $In_xGa_{1-x}N$ layers on GaN [42–45]. Note, however, that plastic relaxation is observed only locally. Nevertheless, the majority of the interfacial area remains coherently strained as further discussed below.

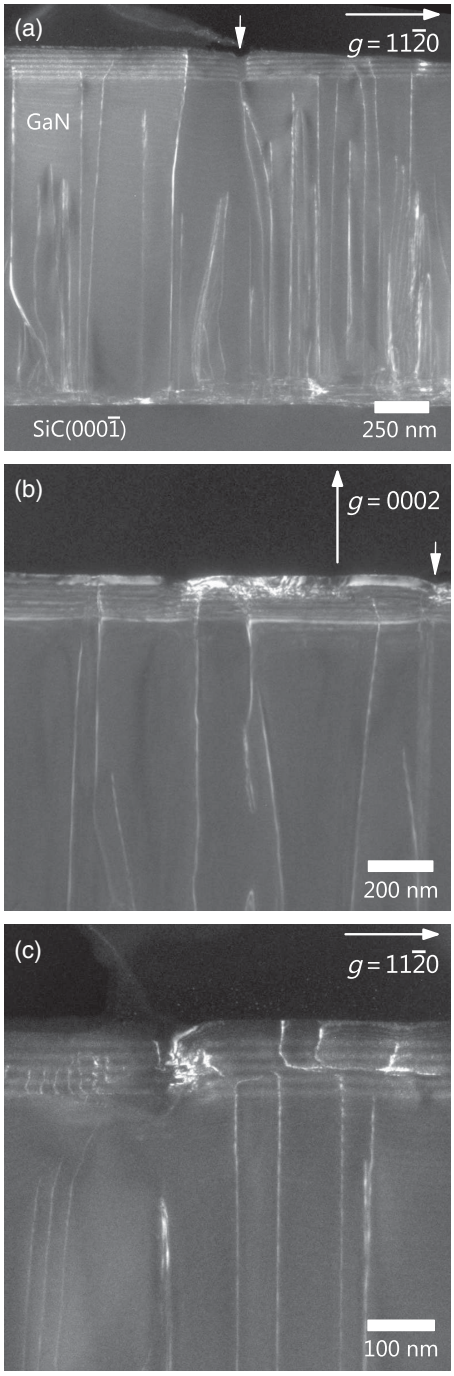

FIG. 7. WBDF micrographs of sample *I* showing the entire sample structure (a) and only the PAMBE grown layers (b) and (c). The diffraction conditions are indicated in each figure. Mixed dislocations are visible in all of the images. *a*-type TDs are visible only in (a) and (c); *c*-type TDs are visible only in (b). The small arrows indicate the position of the ∨-pit defects.

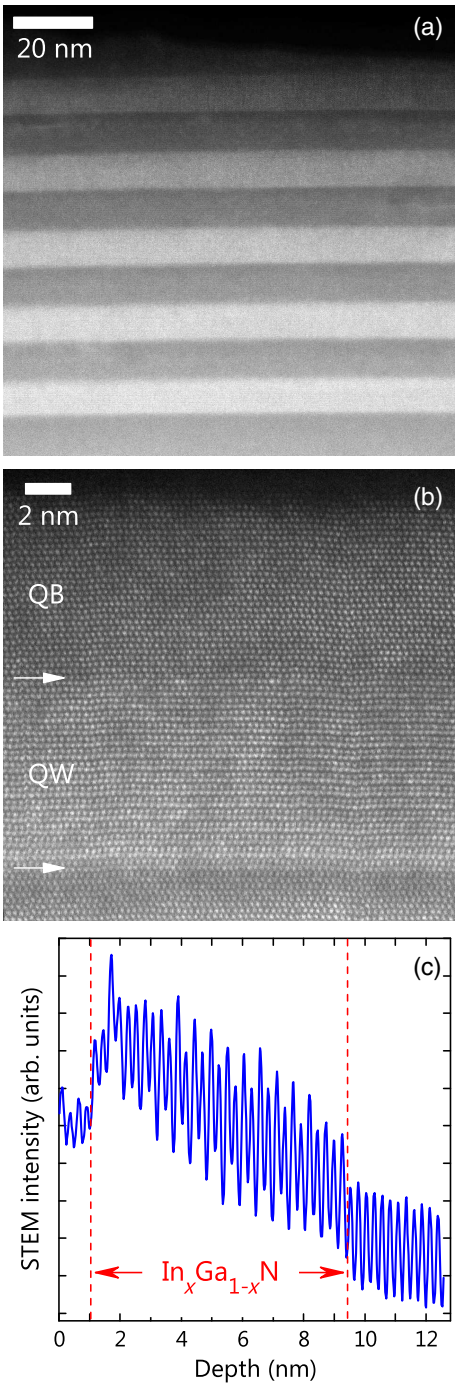

FIG. 8. STEM HAADF micrographs of the entire QW region (a) and the fifth QW (b) of sample *I*. In (b), the arrows indicate the position of the QW or QB interface. Both micrographs were taken along the $[11\bar{2}0]$ direction. (c) STEM HAADF intensity profile along the growth direction for the fifth QW. The red dashed lines indicate the interfaces between the QW and the QBs.

Also note that we do not observe any MDs for sample *G* (not shown here).

Figure 8 shows STEM HAADF images of the QW region of sample *I* taken in a region free from ∨ pits and MDs, where the QWs exhibit a planar morphology. High-resolution STEM HAADF images [Fig. 8(b)] do not show any indication for fluctuations in the In content along the basal (0002) plane. The intensity profile along the growth direction displayed in Fig. 8(c) shows that both the lower and the upper interfaces between the QW and the

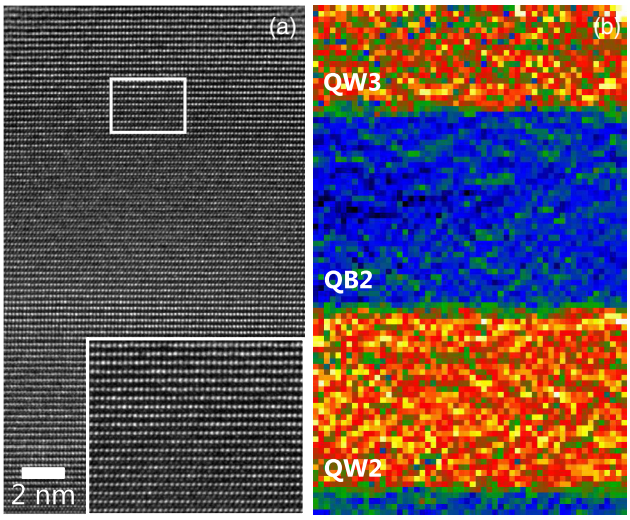

FIG. 9. (a) HRTEM image of the QW region of sample *I* taken along the $[1\bar{1}00]$ direction. The inset shows with higher magnification the interface between the third QW and the subsequent QB. (b) Color-coded map of the local lattice parameter *c* distribution ranging from 500 pm (blue) to 550 pm (yellow).

QBs are abrupt on an atomic scale (the linear change in the STEM intensity along the growth direction is due to the continuous variation in the specimen width). The additional increase in the STEM intensity after the abrupt change observed for a depth of 1 nm is not caused by a variation in the In content but is likely to arise from electron dechanneling effects at the interface between the QW and the QB, a well-known phenomenon in STEM HAADF that complicates the quantitative analysis of STEM intensity profiles [46,47]. This conclusion is supported by the further analysis of the samples by HRTEM (see below). These results also allow us to conclude that the broadening of the satellite peaks observed in the HRXRD profiles [Fig. 4(b)] is, thus, not related to microscopic interface roughness. Finally, as shown in Fig. 8(b), the QW contains 31 atomic planes of $In_xGa_{1-x}N$. The widths of the QWs from samples *G* and *I* as measured by STEM HAADF are 3 and 8.4 nm, respectively.

We analyze the same region of sample *I* by HRTEM in order to further examine the crystal quality of the active region and, in particular, to check the compositional fluctuations of the $In_xGa_{1-x}N/In_yGa_{1-y}N$ QWs. Figure 9(a) presents a HRTEM image of the second and third QWs from sample *I*. A Fourier filtered image (not shown here) confirms the absence of extended defects, such as misfit dislocations or stacking faults, within this region.

Figure 9(b) shows the distribution of the local lattice parameter *c* extracted from a series of HRTEM images similar to the one shown in Fig. 9(a). The local lattice parameter is obtained using the algorithm developed in Ref. [48]. Since the QWs are coherently strained, the local lattice parameter *c* reflects the distribution of the In content inside the QWs. In order to check the compositional uniformity, we construct histograms of the lattice parameter

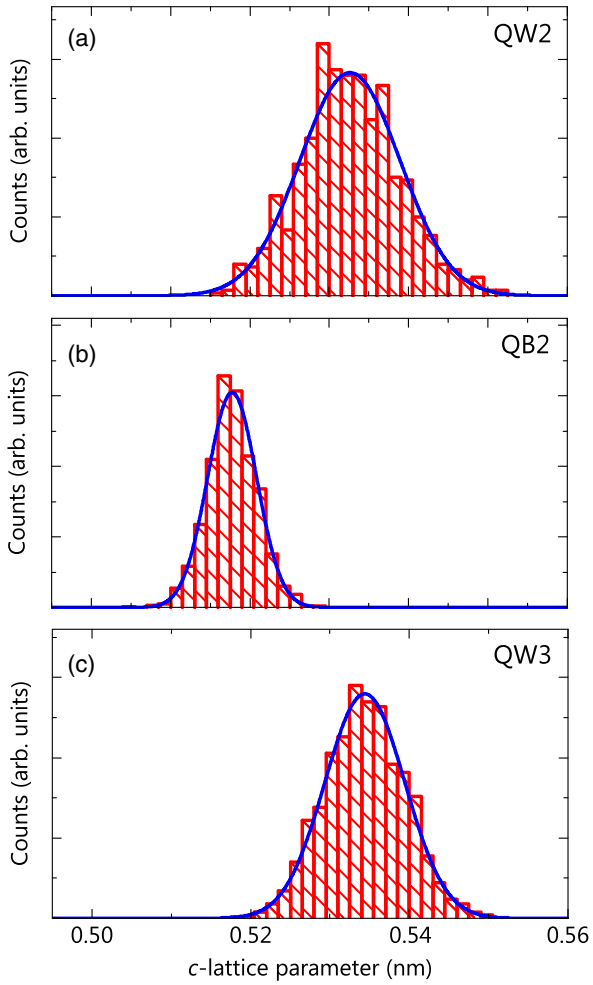

FIG. 10. Histograms of the local lattice parameter *c* measured in a QB and two different QWs of sample *I*. The solid blue lines represent Gaussian fits to the experimental data.

c for two QWs and one QB from sample *I* as shown in Fig. 10. For both QWs and the QB, the histograms are well described by Gaussian distributions indicating that the In distribution in our N-polar $In_xGa_{1-x}N/In_yGa_{1-y}N$ QWs is essentially random [48]. Hence, the anomalous dependence of emission energy and intensity cannot be ascribed to carrier localization by strong, nonrandom alloy fluctuations.

4. Cathodoluminescence

To elucidate the microscopic origin of the luminescence, we examine the samples simultaneously by SEM and low-temperature (10 K) CL. Figures 11(a) and 11(b) show, for comparison, the superposition of the scanning electron micrographs with the monochromatic CL maps for samples *C* and *G*, respectively, for representative spectral windows centered around the peak of the $In_xGa_{1-x}N$ emission band. For the Ga-polar sample *C* [Fig. 11(a)], the surface is flat and smooth, in good agreement with the AFM measurements. The $In_xGa_{1-x}N$-related CL signal is distributed rather uniformly over the entire surface.

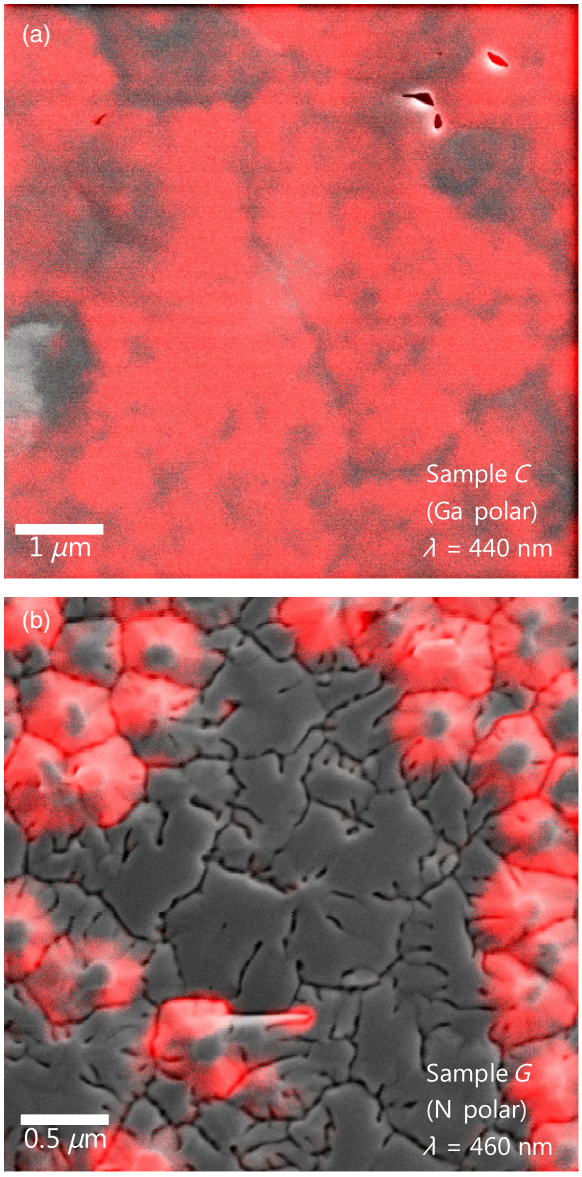

FIG. 11. Representative top-view monochromatic CL and superimposed SEM images of Ga- (a) and N-polar (b) $In_xGa_{1-x}N/In_yGa_{1-y}N$ QWs. The images shown are taken from samples *C* (a) and *G* (b). The CL images are taken at 10 K. For the N-polar sample *G*, the luminescence observed stems exclusively from the semipolar facets formed around TDs.

The surface of the N-polar sample *G* [Fig. 11(b)] consists of flat and smooth $(000\bar{1})$ facets separated by narrow trenches. In addition, a high density of $\vee$ pits is visible which is seen to have the shape of an inverted pyramid with semipolar facets. The superposition of the scanning electron micrograph with the monochromatic CL map reveals that the $In_xGa_{1-x}N$-related luminescence does not originate from the flat and smooth $(000\bar{1})$ facets but from the semipolar facets that constitute the $\vee$-pit defects. In fact, also in monochromatic imaging using other spectral windows or in spectrally resolved measurements on the $(000\bar{1})$ facets (not shown here), we do not observe any CL signal that can be ascribed to the N-polar $In_xGa_{1-x}N/In_yGa_{1-y}N$ QWs. Since each point in the CL images shown in Fig. 11 represents the total intensity integrated over an area of at least $30 \times 30\ \mu m^2$ for this particular point of excitation, regardless of where electrons and holes actually recombine, the lack of luminescence from the flat regions demonstrates that carriers recombine nonradiatively before diffusing towards the $\vee$-pit defects.

Therefore, these results are evidence that the photoluminescence observed from the N-polar samples prepared on $SiC(000\bar{1})$ does not arise from N-polar QWs but from semipolar ones formed in $\vee$-pit defects. The reduced piezoelectric field along semipolar directions [49] partly explains the nonsystematic variation of the PL spectrum when increasing the QW width from sample *G* to *J*. In any case, the understanding of this variation is, at this point, only of secondary importance. The important result here is the lack of luminescence from the flat $(000\bar{1})$ facets that correspond to the regions with well-defined N-polar $In_xGa_{1-x}N/In_yGa_{1-y}N$ QWs. This observation confirms the presence of a highly efficient nonradiative recombination channel within the flat regions of the QWs.

IV. DISCUSSION

If N-polar $In_xGa_{1-x}N/In_yGa_{1-y}N$ QWs are to be used in light-emitting devices, the origin of this nonradiative channel has to be identified and eliminated. Evidently, TD cannot be at the root of this nonradiative channel since N-polar $In_xGa_{1-x}N/In_yGa_{1-y}N$ QWs prepared on freestanding GaN layers (samples studied here and in Ref. [4]) do not exhibit any detectable $In_xGa_{1-x}N$-related luminescence despite having a TD density of only $10^7\ cm^{-2}$. Furthermore, note that our Ga-polar QWs prepared on SiC(0001) substrates (samples *C*–*F*), which have a TD density 3 orders of magnitude higher, exhibit an intense luminescence that as commonly observed, quenches and redshifts with increasing well width due to the quantum confined Stark effect. Misfit dislocations cannot explain our results either because they are not observed in samples *B* and *G*. A higher concentration of nonradiative recombination centers in the bulk of the film associated to the more efficient incorporation of impurities on the $(000\bar{1})$ plane is unlikely because Chèze *et al.* [4] observed an intense luminescence from thick N-polar $In_xGa_{1-x}N$ layers grown under similar conditions as those used for QWs. We, thus, believe that the most plausible explanation left is a high concentration of nonradiative point defects located at the interfaces between QWs and QBs. In fact, it is known for other III–V compound semiconductor heterostructures [50] that point defects can segregate on the growth front and may incorporate at the heterointerface due to the abrupt change of electrochemical potential. This mechanism is particular to a given surface and may result in very high point defect densities at either the normal or the inverted interface between two materials. A high density of

nonradiative point defects at either the $In_xGa_{1-x}N/In_yGa_{1-y}N(000\bar{1})$ or the $In_yGa_{1-y}N/In_xGa_{1-x}N(000\bar{1})$ interface is compatible with all experimental results reported in Ref. [4] and the present work.

Our results and those reported in Ref. [4] contrast with the successful fabrication of N-polar $In_xGa_{1-x}N$ LEDs by Akyol *et al.* [13]. However, these authors did not analyze the microscopic origin of the electroluminescence from their devices. The emission may, thus, have originated from semipolar QWs formed around ∨ pits as observed in the present work or around hillocks as reported in Ref. [15]. Our work provides clear evidence that it must not be taken for granted that the luminescence from a sample containing N-polar $In_xGa_{1-x}N/In_yGa_{1-y}N$ QWs actually stems from these QWs. To ensure that this luminescence is not related to semipolar QWs formed at ∨ pits or to other types of structural defects, these structures have to be examined in detail by microscopic techniques.

The unexpected luminescence quenching observed in N-polar $In_xGa_{1-x}N/In_yGa_{1-y}N$ QWs is not only relevant for the fabrication of LEDs in the form of films but is also of importance for the development of nano-LEDs based on spontaneously formed GaN nanowires (NWs) in PAMBE. As discussed in Refs. [51–53], these nanostructures, if formed spontaneously in the absence of structural or morphological defects of the substrate, elongate along the $[000\bar{1}]$ direction. GaN NWs are, thus, N polar and so are the $In_xGa_{1-x}N$ quantum disks inserted into them. Yet, numerous publications report on the luminescence of these N-polar $In_xGa_{1-x}N$ disks embedded into GaN nanowires [54–58]. While the luminous efficiency of these structures does not seem to be even close to that of planar Ga-polar $In_xGa_{1-x}N$ QWs [55–59], they do luminesce in contrast to the planar QWs studied in the present work. Two essential differences between the $In_xGa_{1-x}N$ disks inserted in GaN NWs and corresponding planar structures may contribute to this fact: first, GaN NWs are formed under N excess [60,61], while planar QWs are grown under metal-stable conditions. The resulting different stoichiometry at the growth front may very well suppress the formation of nonradiative defects during the growth of the $In_xGa_{1-x}N$ quantum disks. Second, $In_xGa_{1-x}N$ disks in GaN NWs have been shown to exhibit large compositional fluctuations [55,57,62] inducing carrier localization, which, in turn, may at least partly prevent nonradiative recombination.

Last, we note that the growth conditions employed here (which are those considered as optimum for the synthesis of N-polar $In_xGa_{1-x}N$ alloys by PAMBE [4,6,13]) are basically identical to the ones commonly used for growing their Ga-polar counterparts. These conditions result in an In-terminated surface which is essential for establishing a two-dimensional growth front on the (0001) surface but may very well result in an enhanced generation of point defects on the $(000\bar{1})$ surface. Here, we investigate N-polar QWs prepared at two substrate temperatures (625 °C and 660 °C) using different growth rates as well as distinct degrees of metal excess (with and without In droplets). In addition, we also analyze N-polar QWs prepared on freestanding GaN layers where In incorporation inside the QBs is completely suppressed (not shown here). Regardless of the changes in these parameters, we always obtain the same result: no detectable luminescence from N-polar QWs. Hence, our results cannot be simply attributed to unsuitable growth conditions but point at a fundamental difference between Ga- and N-polar $In_xGa_{1-x}N/In_yGa_{1-y}N$ heterostructures. In fact, as shown in Ref. [4], our samples prepared on freestanding N-polar GaN layers exhibit an extraordinary structural perfection on par with that of their state-of-the-art Ga-polar counterparts but still do not emit any detectable luminescence. Clearly, further studies are needed to investigate the impact of the surface stoichiometry during growth on the luminous efficiency of N-polar $In_xGa_{1-x}N/In_yGa_{1-y}N$ QWs.

V. SUMMARY AND CONCLUSIONS

We analyze the properties of Ga- and N-polar $In_xGa_{1-x}N/In_yGa_{1-y}N$ QWs grown by PAMBE under nominally identical conditions on different types of substrates. Ga-polar QWs exhibit a strong luminescence. Both the energy and the intensity of the luminescence are largely determined by the QCSE and, thus, by the width of the QWs. In contrast, regardless of the substrate and the QW width, we do not observe luminescence from N-polar QWs. The simulation of the band profiles together with PL measurements carried out with resonant excitation point toward the presence of a very efficient nonradiative recombination channel within the QWs. Because the luminescence quenching is not observed in thick N-polar $In_xGa_{1-x}N$ layers, the most plausible explanation left for this phenomenon is the incorporation of a high density of nonradiative defects at the interfaces between QWs and QBs. In order to take advantage of the potential benefits of the $[000\bar{1}]$ orientation for the fabrication of green LEDs, it is necessary to develop growth approaches designed to eliminate the nonradiative defects in N-polar $In_xGa_{1-x}N/In_yGa_{1-y}N$ QWs.

ACKNOWLEDGMENTS

We thank Hans-Peter Schönherr for his dedicated maintenance of the MBE system, Carsten Pfüller for valuable technical assistance, and Henning Riechert for a critical reading of the manuscript. Partial financial support from the European Union through Grant No. SINOPLE 230765 and by the Polish National Centre for Research and Development Grant No. PBS3/A3/23/2015 is gratefully acknowledged.

[1] L. K. Li, M. J. Jurkovic, W. I. Wang, J. M. Van Hove, and P. P. Chow, Surface polarity dependence of Mg doping in GaN grown by molecular-beam epitaxy, Appl. Phys. Lett. **76**, 1740 (2000).

[2] H. M. Ng and A. Y. Cho, Investigation of Si doping and impurity incorporation dependence on the polarity of GaN by molecular beam epitaxy, J. Vac. Sci. Technol. B **20**, 1217 (2002).

[3] H. Masui, S. Keller, N. Fellows, N. A. Fichtenbaum, M. Furukawa, S. Nakamura, U. K. Mishra, and S. P. DenBaars, Luminescence characteristics of N-polar GaN and InGaN films grown by metal organic chemical vapor deposition, Jpn. J. Appl. Phys. **48**, 071003 (2009).

[4] C. Chèze, M. Siekacz, G. Muzioł, H. Turski, S. Grzanka, M. Kryśko, J. L. Weyher, M. Boćkowski, C. Hauswald, J. Lähnemann, O. Brandt, M. Albrecht, and C. Skierbiszewski, Investigation on the origin of luminescence quenching in N-polar (In,Ga)N multiple quantum wells, J. Vac. Sci. Technol. B **31**, 03C130 (2013).

[5] M. H. Wong, S. Keller, S. Dasgupta Nidhi, D. J. Denninghoff, S. Kolluri, D. F. Brown, J. Lu, N. A. Fichtenbaum, E. Ahmadi, U. Singisetti, A. Chini, S. Rajan, S. P. DenBaars, J. S Speck, and U. K. Mishra, N-polar GaN epitaxy and high electron mobility transistors, Semicond. Sci. Technol. **28**, 074009 (2013).

[6] D. N. Nath, E. Gür, S. A. Ringel, and S. Rajan, Molecular beam epitaxy of N-polar InGaN, Appl. Phys. Lett. **97**, 071903 (2010).

[7] G. Koblmüller, C. S. Gallinat, and J. S. Speck, Surface kinetics and thermal instability of N-face InN grown by plasma-assisted molecular beam epitaxy, J. Appl. Phys. **101**, 083516 (2007).

[8] S.-H. Han, D.-Y. Lee, J.-Y. Lim, J. W. Lee, D.-J. Kim, Y. S. Kim, S.-T. Kim, and S.-J. Park, Effect of internal electric field in well layer of InGaN/GaN multiple quantum well light-emitting diodes on efficiency droop, Jpn. J. Appl. Phys. **51**, 100201 (2012).

[9] R. D. Dupuis, Epitaxial growth of III-V nitride semiconductors by metalorganic chemical vapor deposition, J. Cryst. Growth **178**, 56 (1997).

[10] E. Iliopoulos, A. Georgakilas, E. Dimakis, A. Adikimenakis, K. Tsagaraki, M. Androulidaki, and N. T. Pelekanos, InGaN (0001) alloys grown in the entire composition range by plasma assisted molecular beam epitaxy, Phys. Status Solidi A **203**, 102 (2006).

[11] P. Aseev, P. E. D. Soto Rodriguez, V. J. Gómez, N. U. H. Alvi, J. M. Mánuel, F. M. Morales, J. J. Jiménez, R. García, A. Senichev, C. Lienau, E. Calleja, and R. Nötzel, Near-infrared emitting In-rich InGaN layers grown directly on Si: Towards the whole composition range, Appl. Phys. Lett. **106**, 072102 (2015).

[12] C. A. M. Fabien, B. P. Gunning, W. A. Doolittle, A. M. Fischer, Y. O. Wei, H. Xie, and F. A. Ponce, Low-temperature growth of InGaN films over the entire composition range by MBE, J. Cryst. Growth **425**, 115 (2015).

[13] F. Akyol, D. N. Nath, E. Gür, P. S. Park, and S. Rajan, N-polar III-nitride green (540 nm) light emitting diode, Jpn. J. Appl. Phys. **50**, 052101 (2011).

[14] S. Keller, N. A. Fichtenbaum, M. Furukawa, J. S. Speck, S. P. DenBaars, and U. K. Mishra, Growth and characterization of N-polar InGaN/GaN multiquantum wells, Appl. Phys. Lett. **90**, 191908 (2007).

[15] J. Song, S.-P. Chang, C. Zhang, T.-C. Hsu, and J. Han, Significantly improved luminescence properties of nitrogen-polar $(000\bar{1})$ InGaN multiple quantum wells grown by pulsed metalorganic chemical vapor deposition, ACS Appl. Mater. Interfaces **7**, 273 (2015).

[16] M. F. Schubert, S. Chhajed, J. K. Kim, E. F. Schubert, D. D. Koleske, M. H. Crawford, S. R. Lee, A. J. Fischer, G. Thaler, and M. A. Banas, Effect of dislocation density on efficiency droop in GaInN/GaN light-emitting diodes, Appl. Phys. Lett. **91**, 231114 (2007).

[17] H. Morkoç, *Handbook of Nitride Semiconductors and Devices* (Wiley-VCH Verlag GmbH & Co. KGaA, Weinheim, Germany, 2008), Vol. 3.

[18] S. Nakamura, Background story of the invention of efficient InGaN blue-light-emitting diodes (Nobel lecture), Rev. Mod. Phys. **87**, 1139 (2015).

[19] B. Heying, R. Averbeck, L. F. Chen, E. Haus, H. Riechert, and J. S. Speck, Control of GaN surface morphologies using plasma-assisted molecular beam epitaxy, J. Appl. Phys. **88**, 1855 (2000).

[20] Z. Gačević, V. J. Gómez, N. García Lepetit, P. E. D. Soto Rodríguez, A. Bengoechea, S. Fernández-Garrido, R. Nötzel, and E. Calleja, A comprehensive diagram to grow (0001)InGaN alloys by molecular beam epitaxy, J. Cryst. Growth **364**, 123 (2013).

[21] M. Siekacz, A. Feduniewicz-Żmuda, G. Cywiński, M. Kryśko, I. Grzegory, S. Krukowski, K. Waldrip, W. Jantsch, Z. Wasilewski, S. Porowski, and C. Skierbiszewski, Growth of InGaN and InGaN/InGaN quantum wells by plasma-assisted molecular beam epitaxy, J. Cryst. Growth **310**, 3983 (2008).

[22] M. Stutzmann, O. Ambacher, M. Eickhoff, U. Karrer, A. Lima Pimenta, R. Neuberger, J. Schalwig, R. Dimitrov, P. J. Schuck, and R. D. Grober, Playing with polarity, Phys. Status Solidi B **228**, 505 (2001).

[23] V. M. Kaganer, O. Brandt, A. Trampert, and K. H. Ploog, X-ray diffraction peak profiles from threading dislocations in GaN epitaxial films, Phys. Rev. B **72**, 045423 (2005).

[24] O. Brandt, R. Muralidharan, P. Waltereit, A. Thamm, A. Trampert, H. von Kiedrowski, and K. H. Ploog, Critical issues for the growth of high-quality (Al,Ga)N/GaN and GaN/(In,Ga)N heterostructures on SiC(0001) by molecular-beam epitaxy, Appl. Phys. Lett. **75**, 4019 (1999).

[25] O. Brandt, P. Waltereit, and K. H. Ploog, Determination of strain state and composition of highly mismatched group-III nitride heterostructures by x-ray diffraction, J. Phys. D **35**, 577 (2002).

[26] G. Snider, 1D Poisson/Schrödinger, University of Notre Dame.

[27] R. Kudrawiec, L. Janicki, M. Gladysiewicz, J. Misiewicz, G. Cywinski, M. Boćkowski, G. Muzioł, C. Chèze, M. Sawicka, and C. Skierbiszewski, Contactless electroreflectance studies of surface potential barrier for N- and Ga-face epilayers grown by molecular beam epitaxy, Appl. Phys. Lett. **103**, 052107 (2013).

[28] C. G. Van de Walle and D. Segev, Microscopic origins of surface states on nitride surfaces, J. Appl. Phys. **101**, 081704 (2007).

[29] P. Schley, R. Goldhahn, A. T. Winzer, G. Gobsch, V. Cimalla, O. Ambacher, H. Lu, W. J. Schaff, M. Kurouchi, Y. Nanishi, M. Rakel, C. Cobet, and N. Esser, Dielectric function and van Hove singularities for In-rich $In_xGa_{1-x}N$

alloys: Comparison of N- and metal-face materials, Phys. Rev. B **75**, 205204 (2007).

[30] P. D. C. King, T. D. Veal, C. E. Kendrick, L. R. Bailey, S. M. Durbin, and C. F. McConville, InN/GaN valence band offset: High-resolution x-ray photoemission spectroscopy measurements, Phys. Rev. B **78**, 033308 (2008).

[31] I. Vurgaftman and J. R. Meyer, Band parameters for nitrogen-containing semiconductors, J. Appl. Phys. **94**, 3675 (2003).

[32] F. Bernardini and V. Fiorentini, Nonlinear macroscopic polarization in III–V nitride alloys, Phys. Rev. B **64**, 085207 (2001).

[33] R. K. Ahrenkiel, in Minority Carriers in III–V Semiconductors: Physics and Applications, *Semiconductors and Semimetals* Vol. 39, edited by R. K. Ahrenkiel and M. S. Lundstrom (Elsevier, New York, 1993), pp. 39–150.

[34] A. Galeckas, J. Linnros, and P. Pirouz, Recombination-Induced Stacking Faults: Evidence for a General Mechanism in Hexagonal SiC, Phys. Rev. Lett. **96**, 025502 (2006).

[35] The much stronger reduction of the electron-hole overlap as compared to the experimental emission intensity is due to the fact that the single-particle approach used by our Schrödinger-Poisson simulations neglects the Coulomb interaction between the electron and hole.

[36] S. Chichibu, T. Azuhata, T. Sota, and S. Nakamura, Spontaneous emission of localized excitons in InGaN single and multiquantum well structures, Appl. Phys. Lett. **69**, 4188 (1996).

[37] Y. Narukawa, Y. Kawakami, M. Funato, S. Fujita, S. Fujita, and S. Nakamura, Role of self-formed InGaN quantum dots for exciton localization in the purple laser diode emitting at 420 nm, Appl. Phys. Lett. **70**, 981 (1997).

[38] J. S. Im, S. Heppel, H. Kollmer, A. Sohmer, J. Off, F. Scholz, and A. Hangleiter, Evidence for quantum-dot-like states in GaInN/GaN quantum wells?, J. Cryst. Growth **189–190**, 597 (1998).

[39] S. Chichibu, K. Wada, and S. Nakamura, Spatially resolved cathodoluminescence spectra of InGaN quantum wells, Appl. Phys. Lett. **71**, 2346 (1997).

[40] K. P. O'Donnell, R. W. Martin, and P. G. Middleton, Origin of Luminescence from InGaN Diodes, Phys. Rev. Lett. **82**, 237 (1999).

[41] S. F. Chichibu, A. Uedono, T. Onuma, B. A. Haskell, A. Chakraborty, T. Koyama, P. T. Fini, S. Keller, S. P. DenBaars, J. S. Speck, U. K. Mishra, S. Nakamura, S. Yamaguchi, S. Kamiyama, H. Amano, I. Akasaki, J. Han, and T. Sota, Origin of defect-insensitive emission probability in In-containing (Al,In,Ga)N alloy semiconductors, Nat. Mater. **5**, 810 (2006).

[42] H. Amano, T. Takeuchi, S. Sota, H. Sakai, and I. Akasaki, Structural and optical properties of nitride-based heterostructure and quantum-well structure, MRS Proc. **449**, 1143 (1996).

[43] C. A. Parker, J. C. Roberts, S. M. Bedair, M. J. Reed, S. X. Liu, and N. A. El-Masry, Determination of the critical layer thickness in the InGaN/GaN heterostructures, Appl. Phys. Lett. **75**, 2776 (1999).

[44] S. Pereira, M. R. Correia, E. Pereira, C. Trager-Cowan, F. Sweeney, K. P. O'Donnell, E. Alves, N. Franco, and A. D. Sequeira, Structural and optical properties of InGaN/GaN layers close to the critical layer thickness, Appl. Phys. Lett. **81**, 1207 (2002).

[45] D. Dobrovolskas, A. Vaitkevičius, J. Mickevičius, Ö. Tuna, C. Giesen, M. Heuken, and G. Tamulaitis, Correlation between structure and photoluminescence properties in InGaN epilayers with thicknesses below and above critical thickness, J. Appl. Phys. **114**, 163516 (2013).

[46] Z. Yu, D. A. Muller, and J. Silcox, Study of strain fields at a-Si/c-Si interface, J. Appl. Phys. **95**, 3362 (2004).

[47] A. Marchewka, D. Cooper, C. Lenser, S. Menzel, H. Du, R. Dittmann, R. E. Dunin-Borkowski, and R. Waser, Determination of the electrostatic potential distribution in $Pt/Fe:SrTiO_3/Nb:SrTiO_3$ thin-film structures by electron holography, Sci. Rep. **4**, 6975 (2014).

[48] T. Schulz, T. Remmele, T. Markurt, M. Korytov, and M. Albrecht, Analysis of statistical compositional alloy fluctuations in InGaN from aberration corrected transmission electron microscopy image series, J. Appl. Phys. **112**, 033106 (2012).

[49] A. E. Romanov, T. J. Baker, S. Nakamura, and J. S. Speck, Strain-induced polarization in wurtzite III-nitride semipolar layers, J. Appl. Phys. **100**, 023522 (2006).

[50] J. Behrend, M. Wassermeier, W. Braun, P. Krispin, and K. H. Ploog, Formation of GaAs/AlAs(001) interfaces studied by scanning tunneling microscopy, Phys. Rev. B **53**, 9907 (1996).

[51] K. Hestroffer, C. Leclere, C. Bougerol, H. Renevier, and B. Daudin, Polarity of GaN nanowires grown by plasma-assisted molecular beam epitaxy, Phys. Rev. B **84**, 245302 (2011).

[52] S. Fernández-Garrido, X. Kong, T. Gotschke, R. Calarco, L. Geelhaar, A. Trampert, and O. Brandt, Spontaneous nucleation and growth of GaN nanowires: Fundamental role of crystal polarity, Nano Lett. **12**, 6119 (2012).

[53] O. Romanyuk, S. Fernández-Garrido, P. Jiříček, I. Bartoš, L. Geelhaar, O. Brandt, and T. Paskova, Non-destructive assessment of the polarity of GaN nanowire ensembles using low-energy electron diffraction and x-ray photoelectron diffraction, Appl. Phys. Lett. **106**, 021602 (2015).

[54] A. Kikuchi, M. Kawai, M. Tada, and K. Kishino, InGaN/GaN multiple quantum disk nanocolumn light-emitting diodes grown on (111) Si substrate, Jpn. J. Appl. Phys. **43**, L1524 (2004).

[55] G. Tourbot, C. Bougerol, A. Grenier, M. Den Hertog, D. Sam-Giao, D. Cooper, P. Gilet, B. Gayral, and B. Daudin, Structural and optical properties of InGaN/GaN nanowire heterostructures grown by PA-MBE, Nanotechnology **22**, 075601 (2011).

[56] M. Wölz, J. Lähnemann, O. Brandt, V. M. Kaganer, M. Ramsteiner, C. Pfüller, C. Hauswald, C. Ning Huang, L. Geelhaar, and H. Riechert, Correlation between In content and emission wavelength of InGaN/GaN nanowire heterostructures, Nanotechnology **23**, 455203 (2012).

[57] G. Tourbot, C. Bougerol, F. Glas, L. F. Zagonel, Z. Mahfoud, S. Meuret, P. Gilet, M. Kociak, B. Gayral, and B. Daudin, Growth mechanism and properties of InGaN insertions in GaN nanowires, Nanotechnology **23**, 135703 (2012).

[58] J. Lähnemann, C. Hauswald, M. Wölz, U. Jahn, M. Hanke, L. Geelhaar, and O. Brandt, Localization and defects in axial (In,Ga)N/GaN nanowire heterostructures investigated by

spatially resolved luminescence spectroscopy, J. Phys. D **47**, 394010 (2014).

[59] O. Marquardt, C. Hauswald, M. Wölz, L. Geelhaar, and O. Brandt, Luminous efficiency of axial In_xGaN_{1-x}/GaN nanowire heterostructures: Interplay of polarization and surface potentials, Nano Lett. **13**, 3298 (2013).

[60] S. Fernández-Garrido, J. Grandal, E. Calleja, M. A. Sánchez-García, and D. López-Romero, A growth diagram for plasma-assisted molecular beam epitaxy of GaN nanocolumns on Si(111), J. Appl. Phys. **106**, 126102 (2009).

[61] S. Fernández-Garrido, V. M. Kaganer, K. K. Sabelfeld, T. Gotschke, J. Grandal, E. Calleja, L. Geelhaar, and O. Brandt, Self-regulated radius of spontaneously formed GaN nanowires in molecular beam epitaxy, Nano Lett. **13**, 3274 (2013).

[62] J. Lähnemann, O. Brandt, C. Pfüller, T. Flissikowski, U. Jahn, E. Luna, M. Hanke, M. Knelangen, A. Trampert, and H. T. Grahn, Coexistence of quantum-confined Stark effect and localized states in an (In,Ga)N/GaN nanowire heterostructure, Phys. Rev. B **84**, 155303 (2011).